Amorphous Aluminum-Based Oxychloride Superionic Conductors via Cation-Oxygen Coupled Modification for Durable High-Rate All-Solid-State Lithium Batteries

Chaozhu Huang,[1, 2] Guobin Zhang,[3] Haichuan Guo,[4,5] Lin Yang,[1, 2] Yitian Feng,[1, 2] Quanyan Man,[1, 2] Qing Zhang,[1, 2] Chi Li,[1, 2] Peng Du,[6] Wanwisa Limphirat,[7] Yongbiao Mu* [1, 2] and Lin Zeng* [1, 2]

[1]Shenzhen Key Laboratory of Advanced Energy Storage, Department of Mechanical and Energy Engineering, Southern University of Science and Technology, Shenzhen 518055, China

[2]SUSTech Energy Institute for Carbon Neutrality, Southern University of Science and Technology, Shenzhen 518055, China

[3]Future Technology School, Shenzhen Technology University, Shenzhen 518118, China

[4]Institute of High Energy Physics, Chinese Academy of Sciences, Beijing, 100049, China

[5]Spallation Neutron Source Science Center, Dongguan, 523803, China

[6]K.H. Kuo Center for Material Characterization, Liaoning Academy of Materials, Shenyang 110000, Liaoning, PR China

[7]Synchrotron Light Research Institute, 111 University Avenue, Muang District, Nakhon Ratchasima 30000, Thailand

E-mail: muyb2021@mail.sustech.edu.cn, zengl3@sustech.edu.cn (Lin Zeng)

Supporting Information

Materials and Methods

Material Synthesis: The raw materials used to synthesize the aluminum-based solid electrolytes Li_3AlCl_6, $Li_3AlCl_3O_{1.5}$, $Li_{2.7}Al_{0.7}M_{0.3}Cl_6$ (M = Zr or Hf) and $Li_{3-X}Al_{1-X}M_xCl_{3+x}O_{1.5-0.5x}$ (M = Zr or Hf, $0.1 \leq x \leq 0.5$) were Li_2O (Macklin, 99.9%), $AlCl_3$ (Aladdin, 99.99%), $ZrCl_4$ (Aladdin, 99.99%), and $HfCl_4$ (Aladdin, 99.99%), which required no further processing. The starting materials for each compound were mixed in stoichiometric ratios within a glove box filled with argon ($H_2O < 0.1$ ppm, $O_2 < 0.1$ ppm). The resulting mixture was placed into a zirconia ball mill jar along with zirconia balls at a ball-to-material ratio of 40:1. The mixture was initially ball-milled at a low speed (100 rpm) for 2 hours to ensure thorough mixing of the precursors, followed by high-speed ball milling (500 rpm). The optimal milling time for the sample is provided in Figure S1. After milling, the product was transferred to the glove box for further processing.

Ion conductivity, activation energy, and electronic conductivity measurements: The ionic conductivities of the solid electrolytes were measured using AC impedance spectroscopy over a frequency range of 1 MHz to 10 Hz, with a perturbation voltage of 10 mV. Electrochemical impedance spectroscopy (EIS) was performed using the Solartron Analytical 1470E electrochemical workstation, (UK). The solid electrolyte powders (140 mg) were cold-pressed into pellets (300 MPa) and sandwiched between two stainless steel rods. The pellet thickness ranged from 0.06 cm to 0.08 cm. Ion conductivity was then measured at various temperatures, and the activation energy (E_a) of the solid electrolyte was calculated using the Arrhenius equation.

$$\sigma T = \sigma_0 \exp\left(-\frac{E_a}{kBT}\right) \quad (1)$$

where σ is ionic conductivity, σ_0 is the Arrhenius prefactor, T is absolute temperature, E_a is the activation energy, and kB is the Boltzmann constant.

The cell assembly process for electronic conductivity measurements was similar with the EIS test. The current responses of the cell were measured at various constant voltages for 30 minutes each. The applied voltage ranged from 0.1 to 0.5 V, with a step size of 0.1 V.

Linear sweep voltammetry (LSV) test: Solid electrolyte powders (SEs) were mixed with vapor-grown carbon fiber (VGCF) in a mass ratio of 7:3 to obtain the composite cathode for LSV tests. 70 mg of SE powders were cold-pressed at 250 MPa for 2 minutes, followed by 10 mg of the composite cathode pressed at 300 MPa for 5 minutes. To prevent side reactions between the halide SEs and lithium anode, 40 mg of $Li_{10}GeP_2S_{12}$ was uniformly dispersed on the other side of the pellet and pressed. LSV measurements were performed using a versatile multichannel potentiostat (Solartron Analytical 1470E) with a positive scan range from open-circuit voltage (OCV) to 5 V and OCV to 0 V. The scan rate was 0.5 mV s^{-1}.

Assembly and electrochemical characterizations of All-Solid-State Lithium Batteries (ASSLBs): ~60 mg of Al-based solid electrolyte were pressed into a 10 mm diameter layer under a pressure of approximately 300 MPa (approximately 0.3-0.4 mm in thickness). Next, a ~5 mg (with an active material loading of ~4.5 mg cm^{-2}) composite

of Al-based SE/sc-NCM83 (single-crystal $LiNi_{0.83}Co_{0.12}Mn_{0.05}O_2$) was evenly coated on one side of the electrolyte layer and pressed under 300 MPa for 5 minutes. To prevent direct contact between the SE and lithium-indium, a ~40 mg $Li_{10}GeP_2S_{12}$ (LGPS) powder sheet was used as an interlayer on the negative electrode side and pressed under 300 MPa for 3 minutes (approximately 0.3 mm in thickness). A Li-In alloy anode (100 μm-thick In foil with a diameter of 9.5 mm stacked with 50 μm-thick Li foil with a diameter of 8 mm) was then placed on the LGPS side, with the resulting internal electrode sandwiched between two stainless steel rods. Finally, a stacking pressure of approximately 75 MPa was applied to the ASSLB for electrochemical testing. All fabrication steps were conducted inside an argon-filled glove box (H_2O, O_2 < 0.1 ppm). Galvanostatic cycling of the ASSLBs was performed within a voltage range of 3.0-4.3 V *vs.* Li/Li^+ using NEWARE battery testing systems, the testing temperature was maintained at 30 °C. The in-situ EIS measurements of ASSLBs were conducted using a Solartron Analytical 1470E system, with a frequency range from 1 MHz to 0.1 Hz and an amplitude of 10 mV. Impedance spectra were recorded intermittently during cycling after equilibration for 5 h. During the impedance measurement, the battery was kept at opening circuit voltage. For the distribution of relaxation times (DRT) calculation, an open Matlab code by Prof. Francesco Giucci was used.[1]

Characterization methods:

XRD patterns of the samples were obtained using a MiniFlex 600 X-ray diffractometer equipped with Cu Kα radiation (λ = 1.5406 Å, 40 kV, 15 mA). Kapton tape was used to cover the sample holder, preventing air exposure. The internal standard method was used to quantify the amorphous content in the samples. LiF (50 wt%) was used as the internal standard and mixed with each sample by hand grinding in an agate mortar. The obtained XRD results were analyzed using Rietveld refinement in GSAS-2.[2] Zr K-edge and Hf L_3-edge XAFS data were collected at 1W1B- XAFS Beamline of Beijing Synchrotron Radiation Facility. Cl K-edge XAS data was obtained at beamline 8 of the Synchrotron Light Research Institute (SLRI), Nakhon Ratchasima, Thailand. The XAS data were processed with Athena and Artemis softwares. The surface morphology of the powder samples and cold-pressed electrolyte sheets was observed using a Sigma 300 field emission scanning electron microscope (SEM). Cryogenic TEM (Titan Krios) images were acquired at 77 K using a Falcon 3 camera, and a low does condition ($\approx$7-10 $e \cdot Å^{-2} \cdot s^{-1}$ × 10 s at a counting model for high-resolution TEM imaging) was applied. X-ray photoelectron spectroscopy (XPS) measurements were conducted on a Thermo Scientific ESCALAB 250Xi system using Al Kα radiation (hυ = 1486.8 eV) as the excitation source. Raman spectra were recorded using a HORIBA LabRAM HR Evolution spectrometer with a 532 nm laser as the excitation source. Atomic force microscopy (AFM, MFP-3D Origin, Oxford Instruments) was employed to characterize the surface morphology and modulus distribution of the aluminum-based solid electrolyte. For the force spectroscopy measurements, AFM probes from Bruker (k = 26 $N \cdot m^{-1}$, f_0

= 300 kHz) were employed, with a loading rate of 400 nm·s^{-1}. Solid-state NMR spectra were recorded on a Bruker AVANCE III (600 MHz) instrument, with a ^{7}Li sampling frequency of 10 kHz, using a single-pulse sequence with a pulse width of 1.8 μs and a sampling delay time of 2 s. The ^{27}Al spectra were collected on a Bruker NEO (600 MHz) instrument with a sampling frequency of 13 kHz.

Price calculation: The raw material cost was estimated using recent market transaction prices of the corresponding precursors. The total material cost was calculated as the weighted sum of the individual raw material prices multiplied by their respective mass fractions in the final composition, according to

$$\text{Cost} = \sum_{i} (\boldsymbol{P_i} \times \boldsymbol{w_i})$$

where $\boldsymbol{P_i}$ represents the market price of raw material $\boldsymbol{i}$, and $\boldsymbol{w_i}$ denotes its mass fraction in LAZCO.

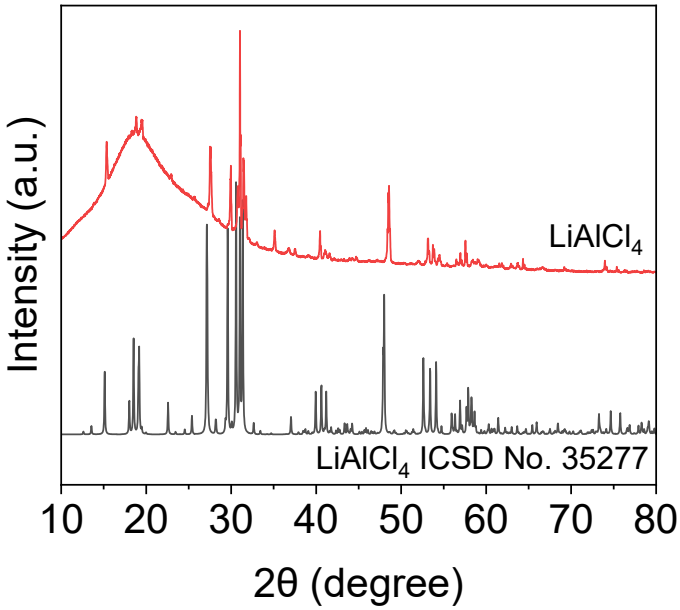

Figure S1. Lab-based XRD patterns of $LiAlCl_4$.

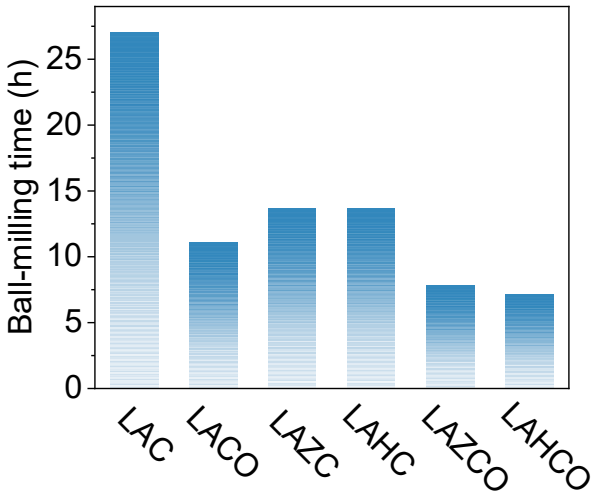

Figure S2. Ball-milling time for achieving the highest ionic conductivity of the Al-based SEs.

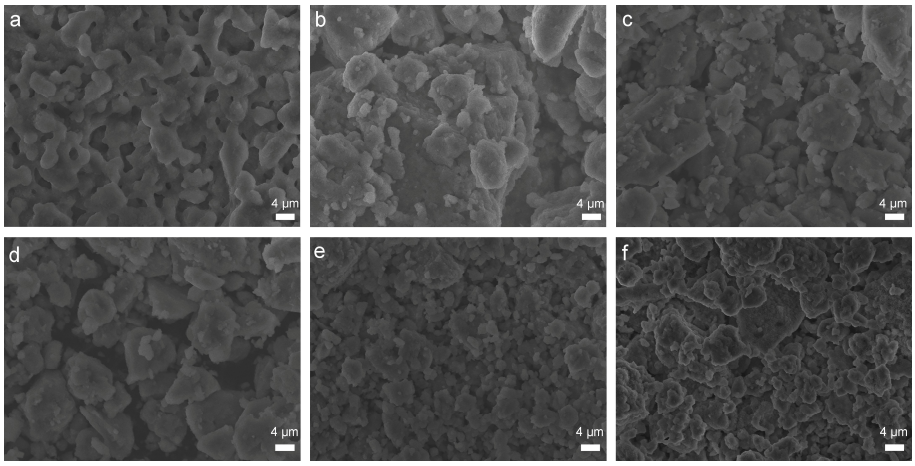

Figure S3. SEM images of the powder: a) LAC, b) LACO, c) LAHC, d) LAZC, e) LAHCO, and f) LAZCO.

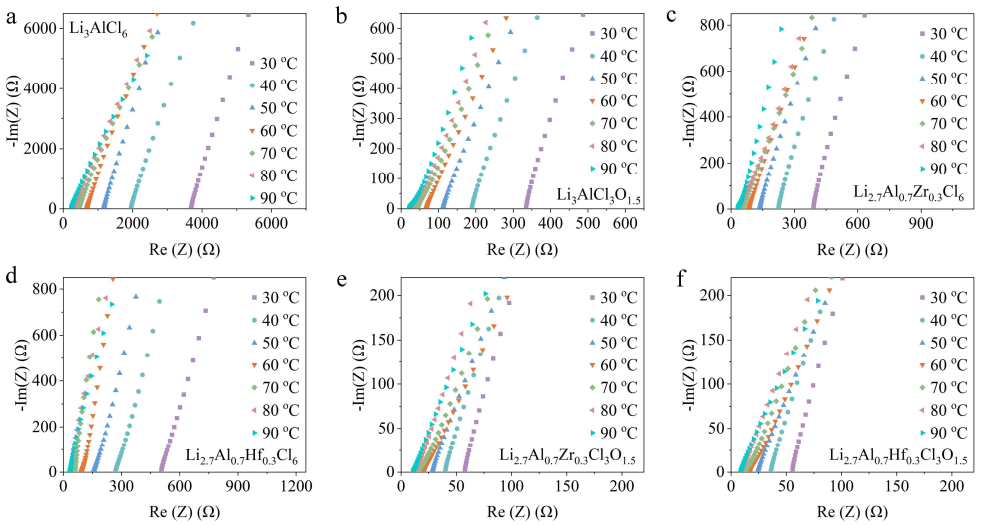

Figure S4. Nyquist plots of a) LAC, b) LACO, c) LAZC d) LAHC e) LAZCO and f) LAHCO at different temperatures.

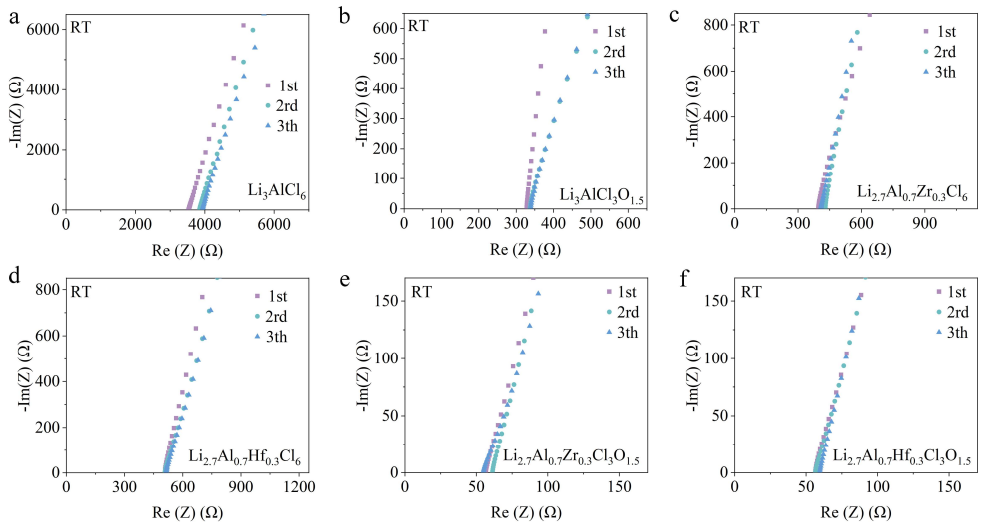

Figure S5. Nyquist plots at room temperature for three independent measurements of a) LAC, b) LACO, c) LAZC, d) LAHC, e) LAZCO, and f) LAHCO.

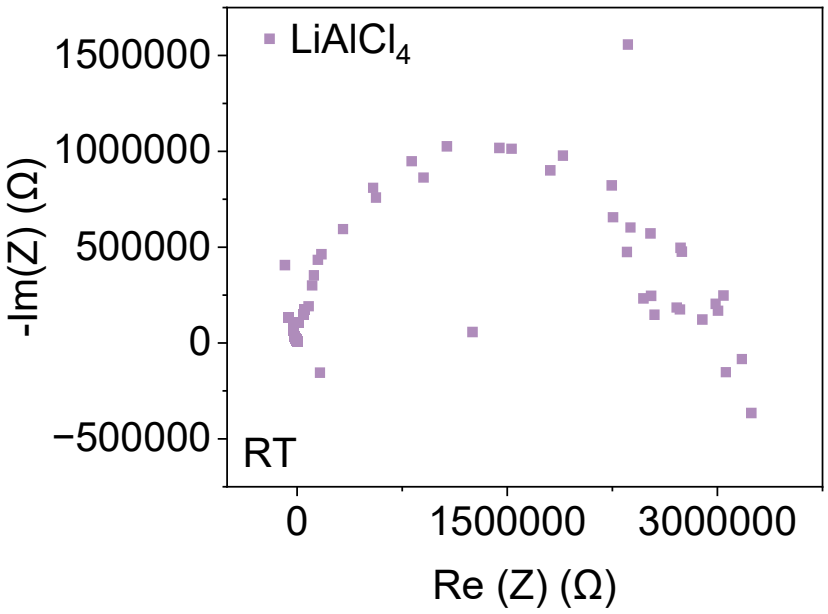

Figure S6. Nyquist plots at room temperature for $LiAlCl_4$.

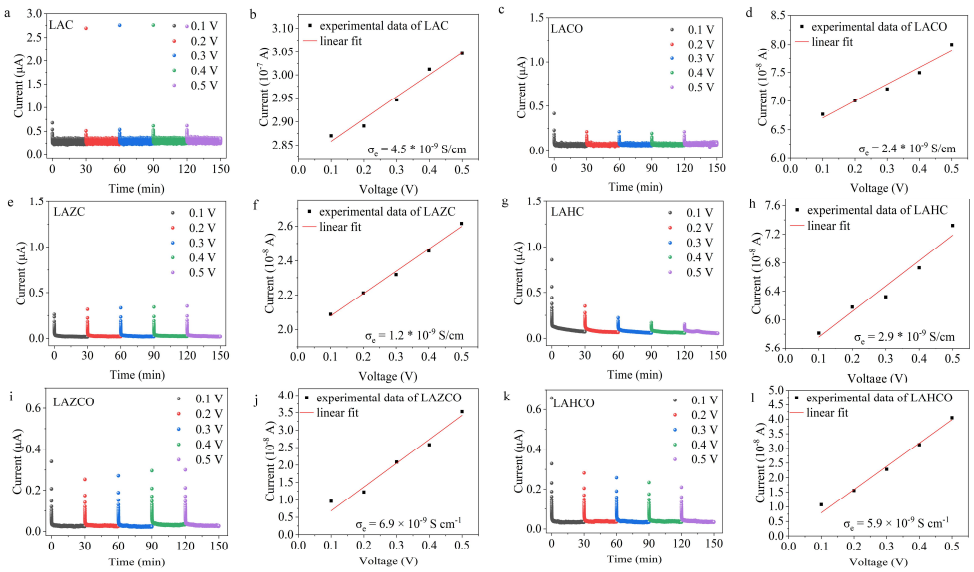

Figure S7. DC polarization curves of a-b) LAC, c-d) LACO, e-f) LAZC, g-h) LAHC, i-j) LAZCO and k-l) LAHCO measured using stainless|SE|stainless symmetric cells at applied voltages from 0.1 to 0.5 V.

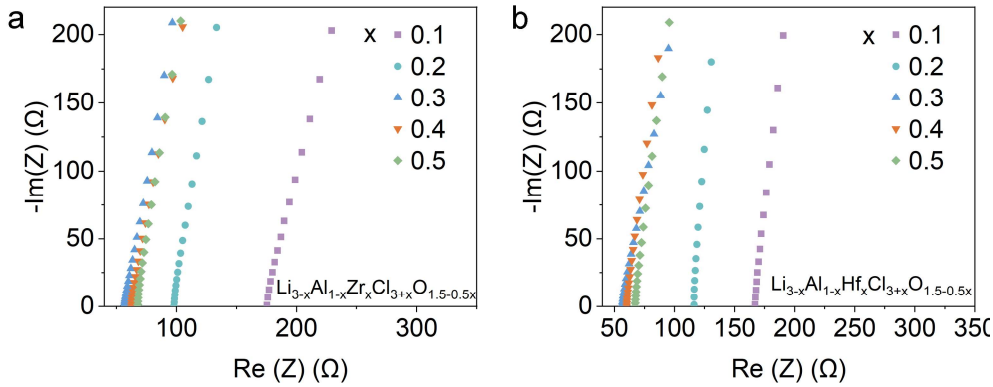

Figure S8. Nyquist plots of a) $Li_{3-x}Al_{1-x}Zr_xCl_{3+x}O_{1.5-0.5x}$ and b) $Li_{3-x}Al_{1-x}Hf_xCl_{3+x}O_{1.5-0.5x}$.

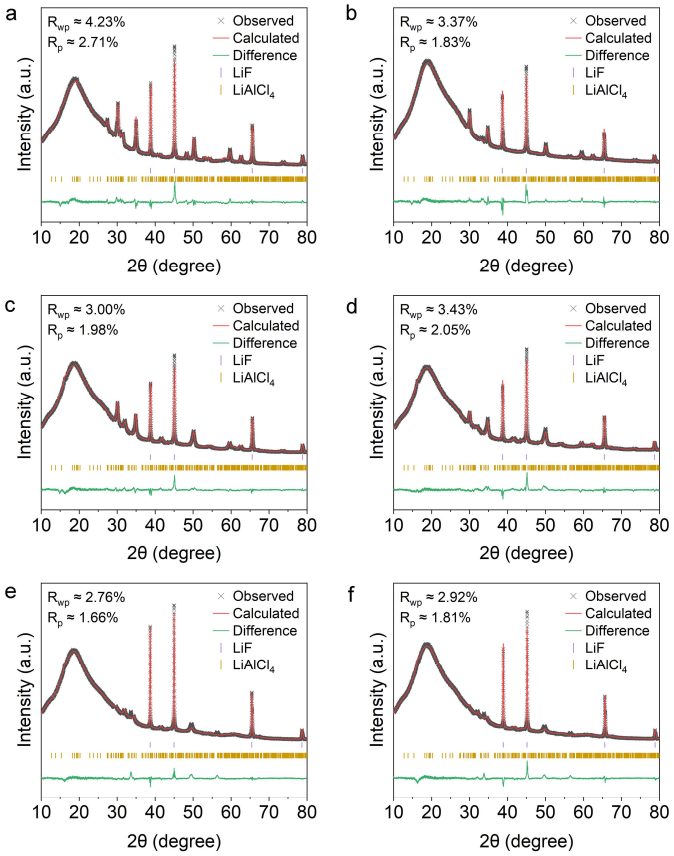

Figure S9. Quantification of the amorphous content in a) LAC, b) LACO, c) LAZC, d) LAHC, e) LAZCO and f) LAHCO using the LiF internal standard method.

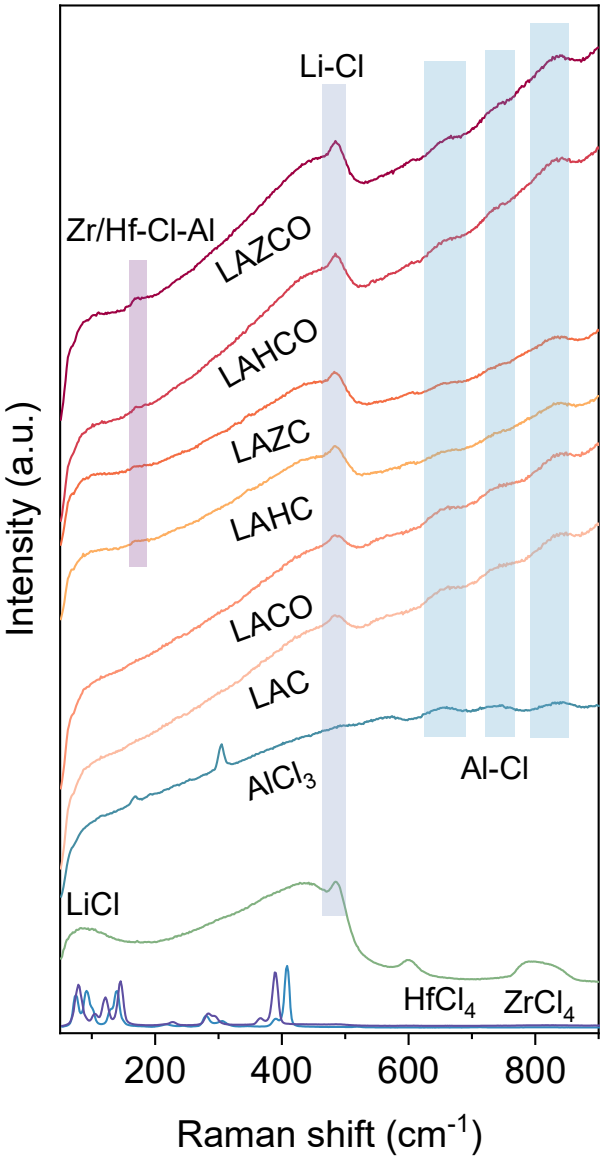

Figure S10. Raman spectra of Al-based SEs, LiCl, $AlCl_3$, $ZrCl_4$ and $HfCl_4$.

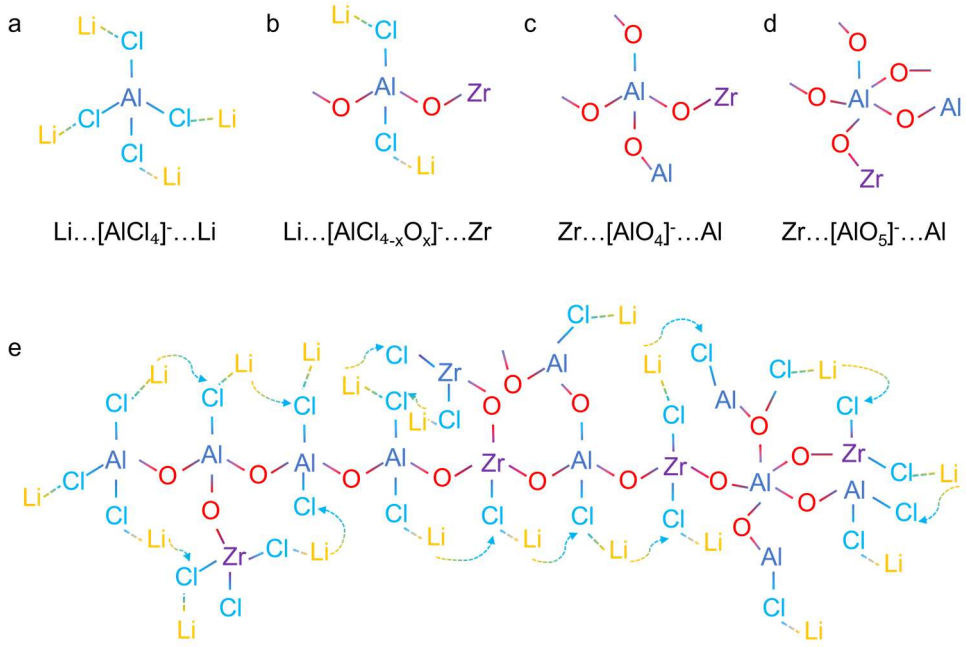

Figure S11. Schematic illustration of several representative local coordination polyhedra and the possible Li^+ transport mechanisms within the three-dimensional amorphous network.

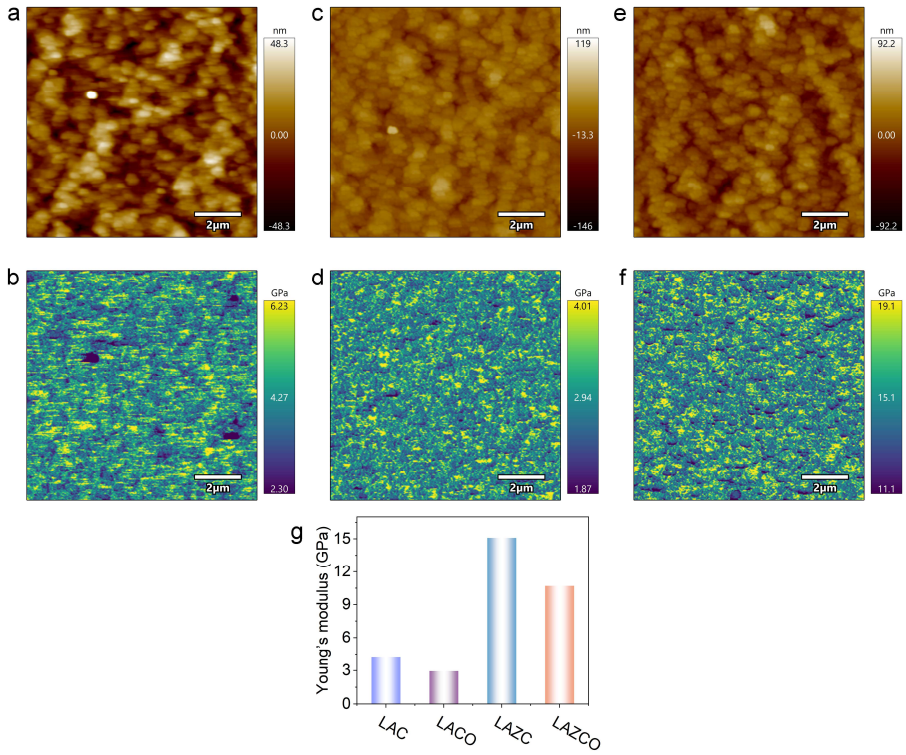

Figure S12. a c e) AFM topography images and b d f) Young's modulus distribution of LAC, LACO and LAZC. g) The average Young's modulus of LAC, LACO, LAZC, and LAZCO.

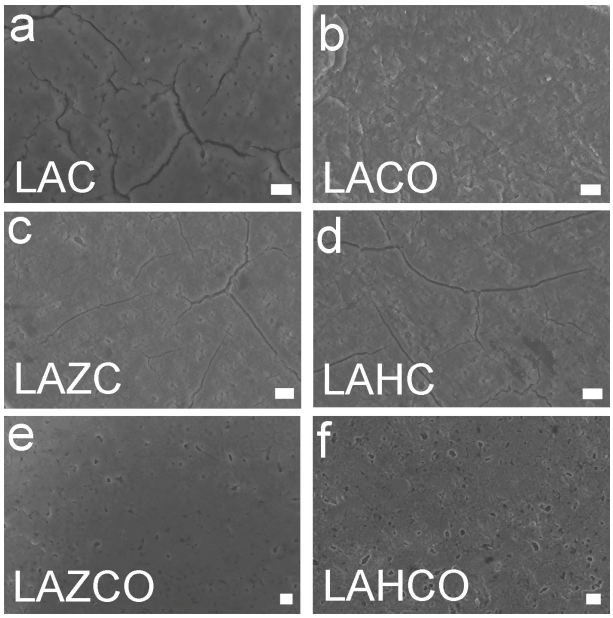

Figure S13. a) LAC, b) LACO, c) LAZC, d) LAHC, e) LAZCO and f) LAHCO solid electrolyte pellets cold-pressed at 300 MPa pressure (scale bars in all images are 5 μm).

As shown in Fig. S13, LAC, LAZC, and LAHC with lower amorphous fractions exhibit pronounced surface cracking after cold pressing, whereas LACO, LAZCO, and LAHCO with higher amorphous fractions display dense and continuous surfaces. These results indicate that high amorphization improves deformability, which may contribute to reduced grain boundary resistance, enhanced electrode-electrolyte contact, and suppressed microcrack formation, thereby supporting stable ASSLB operation under high-rate and long-cycle conditions.

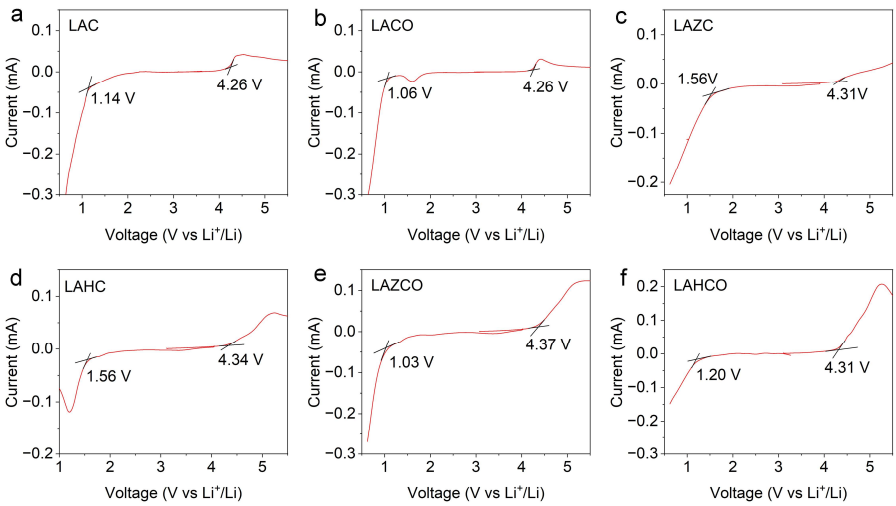

Figure S14. Linear sweep voltammetry (LSV) curve of Li-In|$Li_{10}GeP_2S_{12}$|Al-based SE|Al-based SE-vapor-grown carbon fiber (VGCF) all-solid-state lithium batteries (ASSLBs) at 0.5 mV s^{-1}. a) LAC, b) LACO, c) LAZC, d) LAHC, e) LAZCO and f) LAHCO

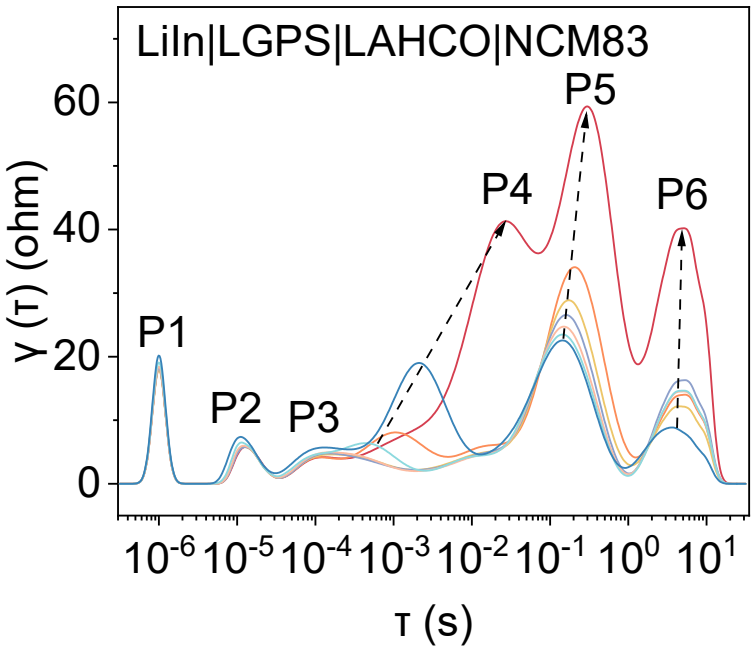

Figure S15. Typical distribution of relaxation time (DRT) curves are calculated from In-situ EIS measurements of LAHCO-based ASSLBs.

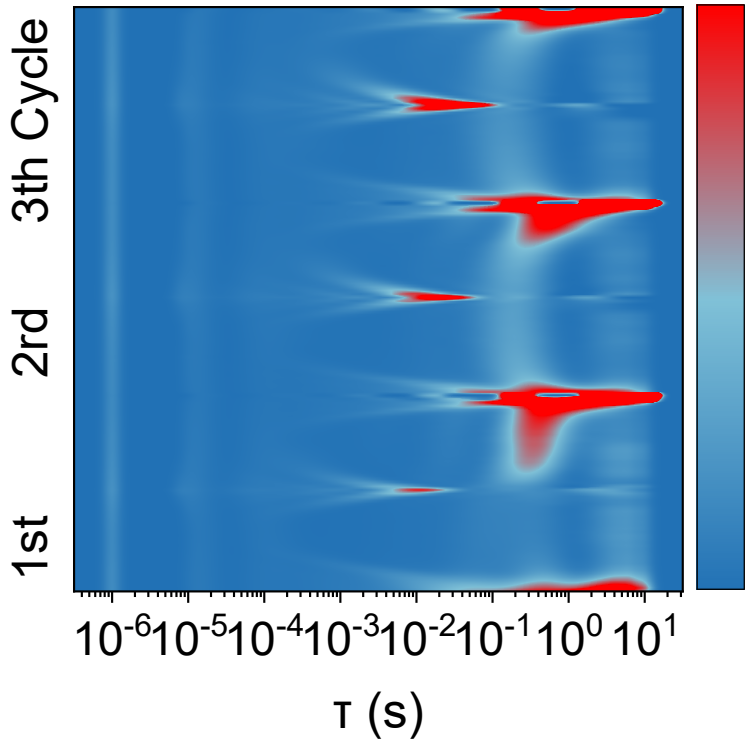

Figure S16. Two-dimensional intensity color maps derived from the DRT curves of the assembled LAHCO-based ASSLBs during charge-discharge cycles (0.05 C, 3.0-4.3 V, three cycles).

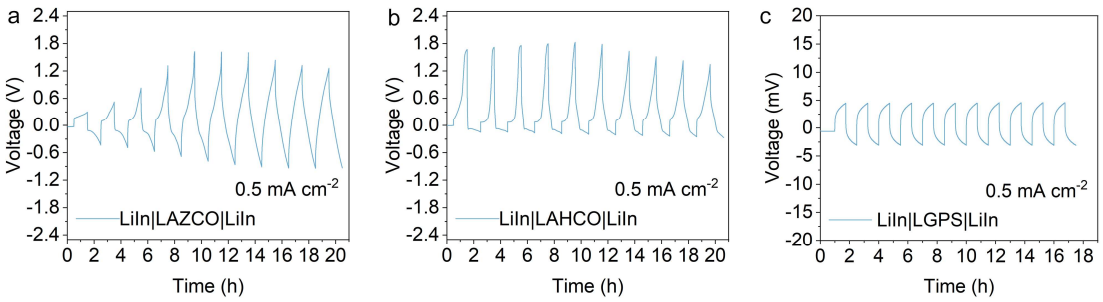

Figure S17. Electrochemical performance of symmetric cells: a) LiIn|LAZCO|LiIn, b) LiIn|LAHCO|LiIn and c) LiIn|LGPS|LiIn.

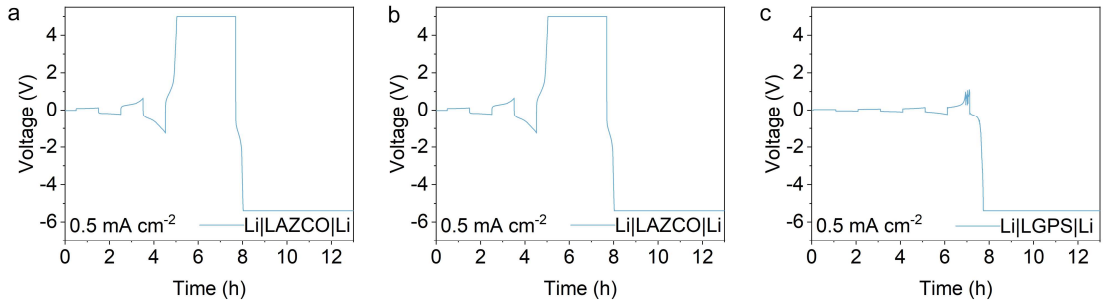

Figure S18. Electrochemical performance of symmetric cells: a) Li|LAZCO|Li, b) Li|LAHCO|Li and c) Li|LGPS|Li.

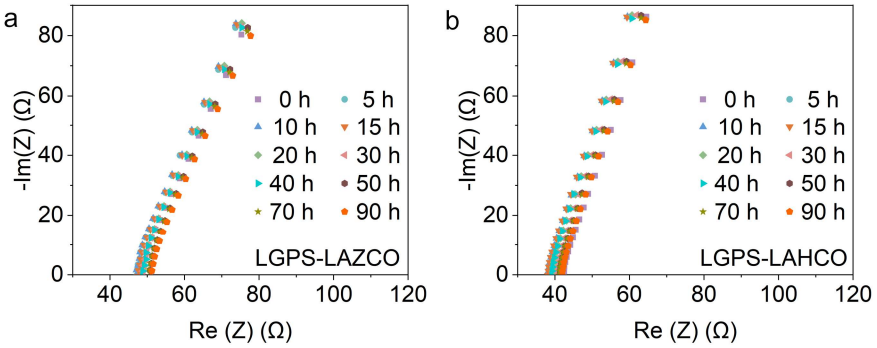

Figure S19. Evaluation of the interfacial stability between LGPS and a) LAZCO, b) LAHCO electrolytes.

To evaluate the interfacial compatibility between the sulfide electrolyte LGPS and aluminum-based oxychloride electrolytes, LGPS was mechanically mixed with LAZCO or LAHCO powders and subsequently pelletized. The ionic conductivity of the mixed pellets was monitored over a period of 0-90 h to probe possible interfacial reactions. As shown in Fig. S19, no noticeable change in ionic conductivity was observed during the testing period, indicating good interfacial stability between LGPS and LAZ(H)CO. These results suggest that no severe interfacial reactions occur at the LGPS–oxychloride electrolyte interface, which is consistent with previous reports on the interfacial compatibility between sulfide and halide-based solid electrolytes.

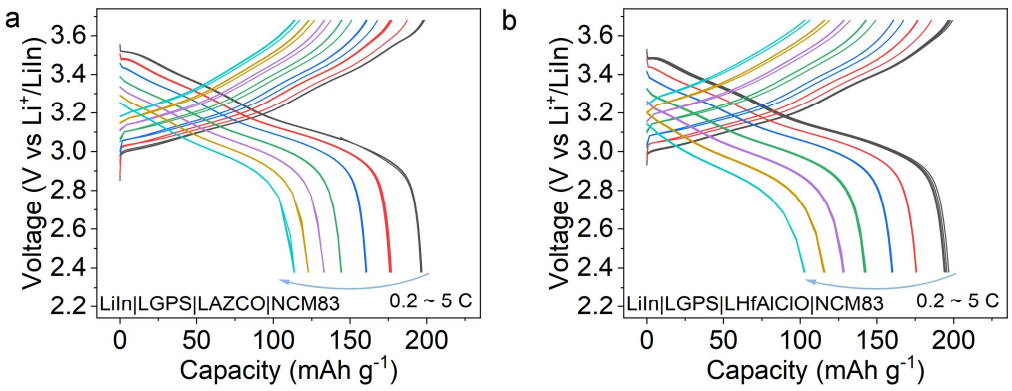

Figure S20. Galvanostatic charge-discharge curves of a) Li-In|LGPS|LAZCO|NCM83 and b) Li-In|LGPS|LAHCO|scNMC83 at various rates from 0.2 to 5 C

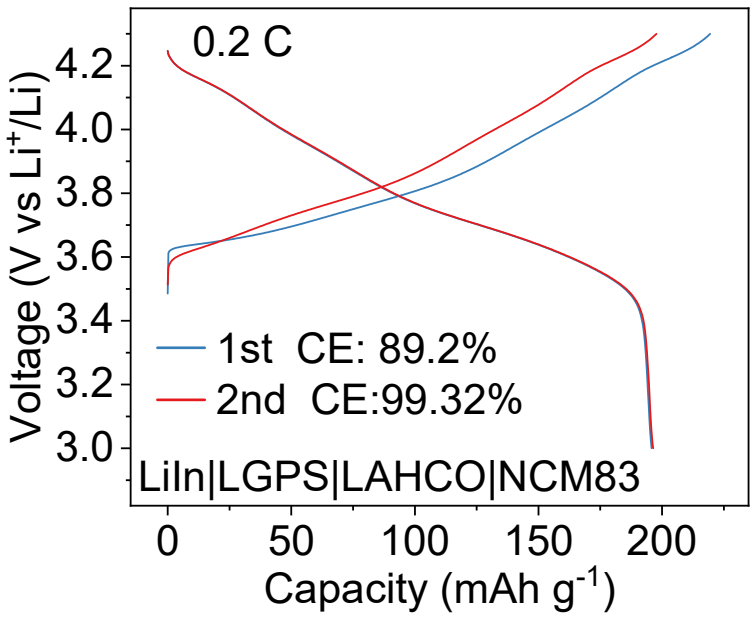

Figure S21. Galvanostatic charge-discharge curves cycled at a rate of 0.2 C in the voltage range of 3.0 - 4.3 V vs Li/Li^+ LAHCO-based ASSLBs.

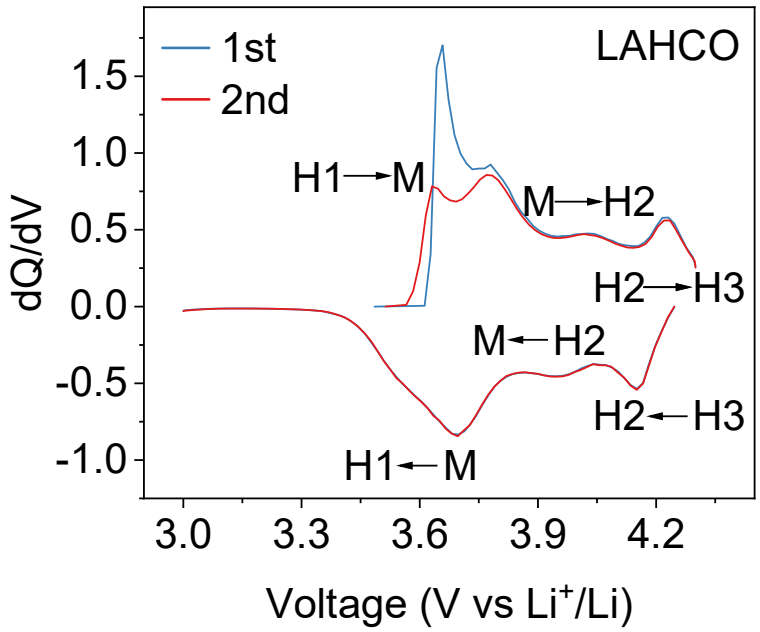

Figure S22. The dQ/dV profiles of LAHCO-based ASSLBs at initial two cycles at 0.1 C.

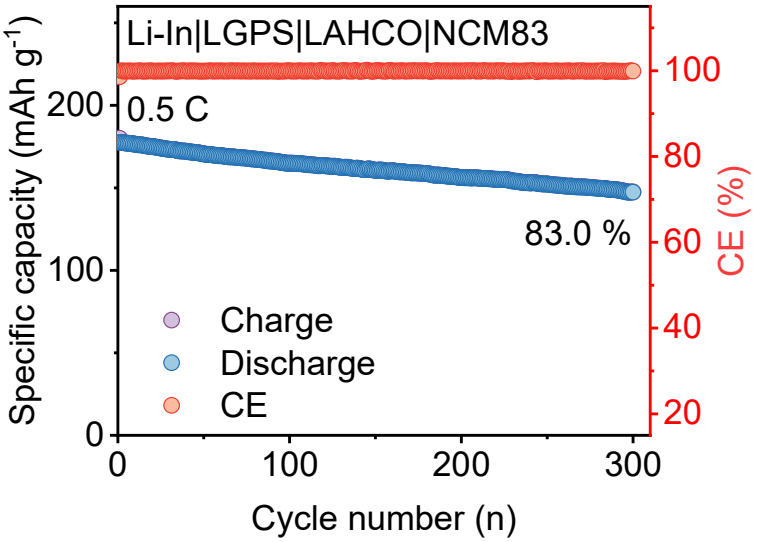

Figure S23. Cycling stability of LAHCO-based ASSLBs at 0.5 C.

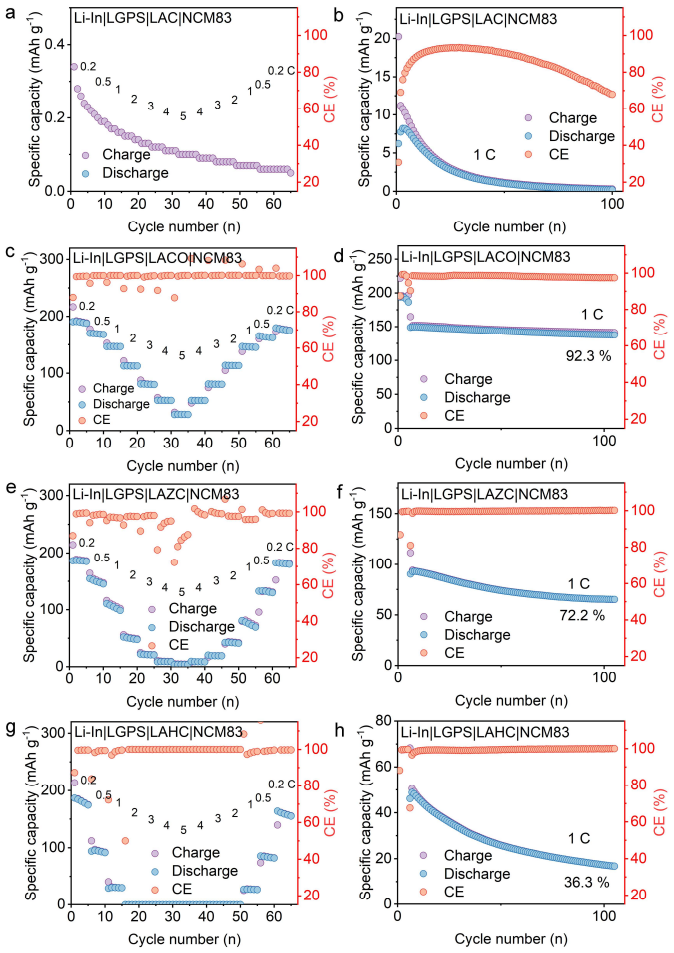

Figure S24. Rate and cycling performance of Li–In|LGPS|SE|NCM83 ASSLBs: a) LAC-, c) LACO-, e) LAHC-, and g) LAZC-based ASSLBs for rate performance from 0.2 to 5 C; and b) LAC-, d) LACO-, f) LAHC-, and h) LAZC-based ASSLBs for cycling performance at 1 C.

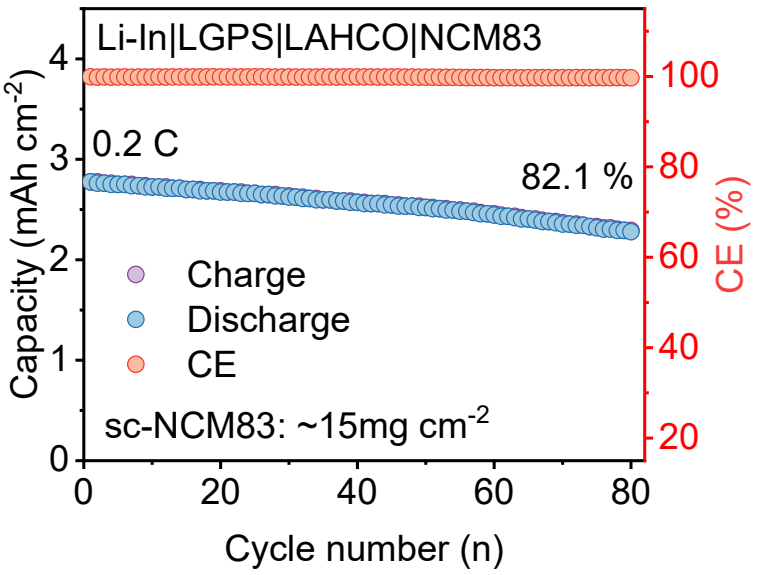

Figure S25. Cycling characteristics of LAHCO-based ASSLBs with a high mass loading of sc-NCM83 (15 mg cm^{-2}) at 0.2 C.

The gravimetric energy density of the all-solid-state cells was evaluated at the cell level by considering the total mass of the anode, electrolyte, and cathode. At 0.2 C and within a voltage window of 3.0-4.3 V, cells with a cathode loading of ~4.5 mg cm^2 exhibited gravimetric energy densities of ~24.1 Wh kg^{-1} for LAZCO and ~23.9 Wh kg^{-1} for LAHCO, corresponding to a total cell mass of ~106 mg. Increasing the cathode loading to ~15 mg cm^{-2} increased the total cell mass to ~120 mg and raised the gravimetric energy densities to ~67.9 Wh kg^1 and ~73.6 Wh kg^{-1}, respectively. The relatively low energy density at the present stage mainly originates from the modest cathode areal loading and excess electrolyte used in this proof-of-concept study, which can be further optimized in future work.

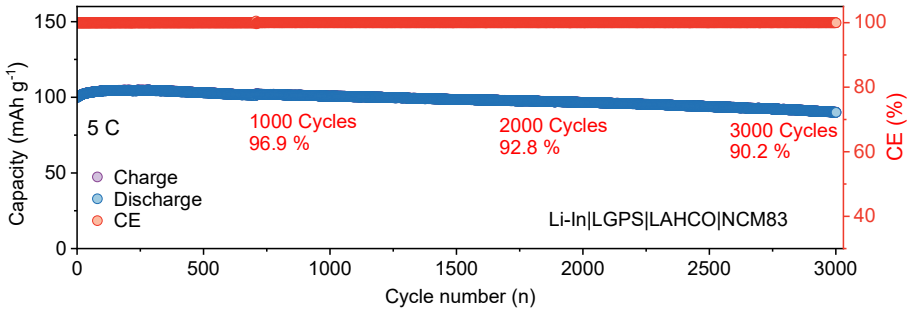

Figure S26. Long-term cycling stability of LAHCO-based ASSLBs under high-rate operation (5 C) within the voltage window of 3.0-4.3 V.

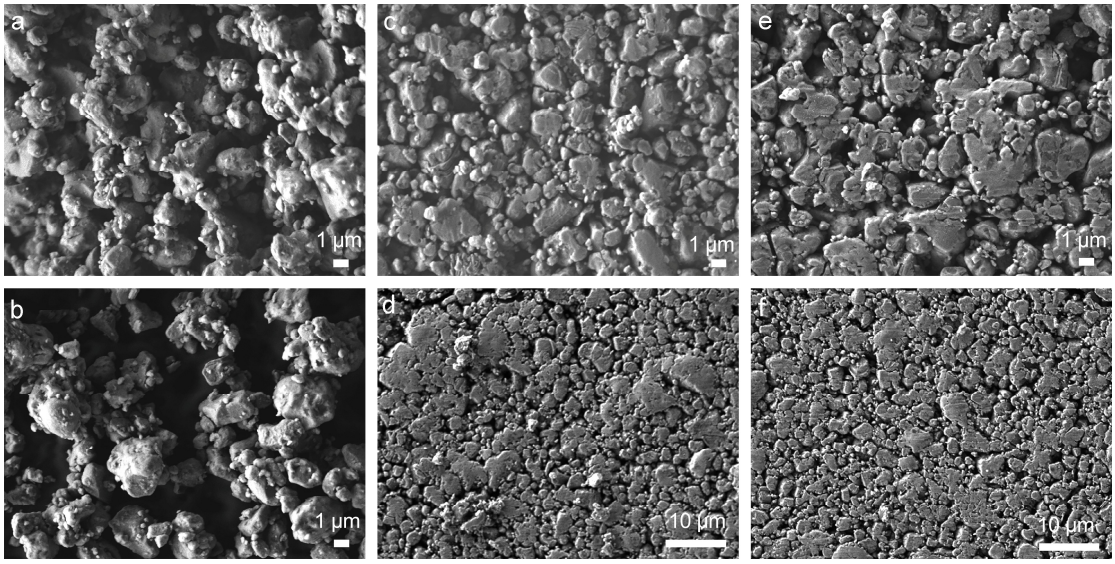

Figure S27. SEM images of cathode composites obtained by mechanically mixing sc-NCM83 with a) LAZCO and b) LAHCO, and the corresponding cathode morphologies of LAZCO-based and LAHCO-based full cells c, d) before cycling and e, f) after cycling.

Table S1 Ionic conductivity at room temperature and corresponding activation energy of Al-based SEs.

Halide SEs	**Ionic conductivity (mS cm^{-1})**	**E_a (eV)**
LAC	0.032	0.45
LACO	0.34	0.44
LAZC	0.28	0.41
LAHC	0.22	0.46
LAZCO	1.63	0.28
LAHCO	1.65	0.31

Table S2 Average market prices of the industrial commodity chemicals in 2024 and the sources from which these prices are acquired.

Commodity chemical	Average market price in 2024 ($ kg-^{1})	Mass fraction in LAZCO (wt %)	Sources
Li_2O	210.67	19.8	CBC Metal (https://www.cbcie.com/) Asian Metal (https://www.asianmetal.cn/) Shanghai Metals Market (https://www.smm.cn/)
$AlCl_3$	0.84	45.8	
$ZrCl_4$	11.24	34.4	

Table S3 Comparison of electrochemical performances of the ASSLBs.

SE	Cathode and Loading (mg)	Electrolyte mass (mg)	Anode interfacial layer (mg)	Rate (C)	Cycles and retention	Ref.
$Li_{1.1}AlO_{1.1}Cl_3$[3]	NCM811, 12.5	120	/	0.1	250, 80%	S4
LiAlOCl	NCM88, 10	45	LPSC, 60	0.5	1500, 85%	22
LiAlOCl-2LiCl	NCM88, 10	60	LPSC, 60	1	1600, 84.9%	21
$Li_3Zr_{0.75}OCl_4$[4]	NCM811, ~3-4	25	LPSC, 55	5	700, 80.9%	S5
$Li_{2.5}ZrCl_5F_{0.5}O_{0.5}$	NCM955, 7	60	LPSC, 40	0.5	500, 81.2%	32
hc-$Li_{2+x}Zr_{1-x}In_xCl_6$[5]	NCM955, 7	60	LPSC, 40	1	500, 74%	S6
$Li_{2.5}Sc_{0.5}Zr_{0.5}Cl_6$[6]	NCM811, 5-7	60	LPSC, 40	0.2	200, 90%	S7
$Li_{2.1}Zr_{0.95}Cu_{0.05}Cl_{4.4}O_{0.8}$	NCM83, 7-9	60	LPSC, 40	2	1000, 90.3%	28
$Li_3ZrCl_4O_{1.5}$	NCM83, 10	60	Li_3YCl_6, 40	1	300, 90.1%	26
$Li_{2.25}Zr_{0.75}Fe_{0.25}Cl_6$	NCM811, /	/	LPSC, 150	0.5	100, 90.5%	29
$1.5Li_2O$-$HfCl_4$	NCM83, 10	60	Li_3YCl_6, 40	0.5	300, 89.6%	27
$Li_{2.5}Y_{0.5}Hf_{0.5}Cl_6$[7]	LCO, 5	70	LPSC, 30	0.1	100, 70%	S8
$Li_{2.1}Zr_{0.95}Mg_{0.05}Cl_6$[8]	LCO, /	/	LPSC, /	0.3	100, 88%	S9
$Li_{2.25}Zr_{0.75}Al_{0.25}Cl_6$	NCM811, 6.8	/	LPSC, /	1	200, 89.6%	25
$1.4Li_2O$-$0.75ZrCl_4$-$0.25AlCl_3$[9]	scNCM92, 5.29	25	LPSC, 35	0.33	200, 82.06%	S9
$Li_2(Zr^{4+}_aZr^{3+}_bZr^{2+}_c)^{(4-3x)+}In^{3+}_xCl_6$ ($0 < x < 1/3$, $a + b + c = 1$)[10]	LCO, 5	60	LPSC, 30	0.5	300, 78.7%	S10
$Li_{2-x}Ta_xZr_{1-x}Cl_6$[11]	NCM811, 5	120	Li_3YCl_6, /	1	100, 80.2%	S11
oh-LZC[12]	LCO, /	/	LPSC, /	0.5	450, 80%	S12

LAZCO	NCM83, 5	60	LGPS, 40	1	500, 90.6%	This work
		60	LGPS, 40	5	4000, 90.3%	
	NCM83, ~17	60	LGPS, 40	0.2	100, 89%	
LAHCO	NCM83, 5	60	LGPS, 40	5	3000, 90.2%	

References

1. T. H. Wan, M. Saccoccio, C. Chen and F. Ciucci, *Electrochimica Acta*, 2015, **184**, 483-499.
2. B. H. Toby and R. B. Von Dreele, *Journal of Applied Crystallography*, 2013, **46**, 544-549.
3. W. Kim, S. Han, S. Lee, J. Yoo, C. Park, S. Yu, D. Won, E. Lee, K.-h. Ko, J. Noh, G. Choi, M. Kim and K. Kang, *Energy Environ. Sci.*, 2025, **18**, 8039-8051.
4. J. Wang, F. Chen, L. Hu and C. Ma, *Nano Lett.*, 2023, **23**, 6081-6087.
5. K. Wang, Z. Gu, H. Liu, L. Hu, Y. Wu, J. Xu and C. Ma, *Adv. Sci.*, 2024, **11**, e2305394.
6. W. Li, Z. Chen, Y. Chen, W. Duan, G. Liu, Y. Lv, H. Yang and L. Yao, *Chem. Eng. J.*, 2023, **455**, 140509.
7. K. Tuo, C. Sun, C. A. López, M. T. Fernández-Díaz and J. A. Alonso, *J. Mater. Chem. A*, 2023, **11**, 15651-15662.
8. H. Zhang, Z. Yu, H. Chen, Y. Zhou, X. Huang and B. Tian, *J. Energy Chem.*, 2023, **79**, 348-356.
9. L. Hu, Y. He, D. Wang, W. Li, J. Yao, X. Zhang, J. Zhu, H. Chen, W. Yin, Y. Wang, K. Yan, J. Wang, H. Li, F. Chen, Y. Liu, J. Lai, Q. Chen, J. Ma, S. Jiao, G. Wang, S. Shi, L. Chen, J. Huang and C. Ma, *Nature Communications*, 2026, **17**.
10. S. Sun, R. Zhang, Z. Gu, X. Fang, T. Ma, H. Li, Z. Lin, H. Yi, X. Zhang, L. Wu, K. Sun, D. Liu, Y. Wu, H. Ma, Y. Fu, K. Wang and D. He, *Adv. Energy Mater.*, 2025, **15**, 2500390.
11. L. Gao, Z. Zhang, Z. Zhang, Y. Luo, B. Hong, L. Di, H. Ni, J. Zhu, R. Zou, E. Zhao and S. Han, *Adv. Funct. Mater.*, 2025, DOI: 10.1002/adfm.202519648, e19648.
12. Y. Zhang, Q. Meng, A. Zeng, S. Qiu, H. Zhang, E. Zhao and X. Xiao, *Angew. Chem. Int. Ed.*, 2025, **65**, e16259.